Are Topological Insulators Promising Thermoelectrics?

Michael Y. Toriyama[a*] and G. Jeffrey Snyder[a*]

Some of the best thermoelectric (TE) materials to date are also topological insulators (TIs). While many studies have investigated the effects of topologically-protected surface states on TE properties, the conditions needed to realize such effects are quite different from typical operating conditions of TE devices for, *e.g.*, power generation and room-temperature Peltier cooling. As a result, it is still unclear what properties of TIs, especially those related to the bulk band structure, are beneficial for TE performance, if any. Here, we perform high-throughput transport calculations using density functional theory (DFT) to reveal that, within the same structure type, TIs tend to outperform normal insulators as TEs when properly optimized. The calculations also indicate that the TE performance is higher for TIs with strongly inverted bands. To explain these observations, we develop models based on Boltzmann transport theory which show that warping driven by band inversion, a key characteristic of TIs, is responsible for the high TE performance of TIs. We find that warping benefits the TE performance because of reduced transport mass and effectively higher valley degeneracy. Our results show that the band inversion strength is a critical property of a TI dictating the TE performance, and we suggest potential strategies to tune the inversion strength and enhance the TE performance in TIs, such as alloying and strain engineering. The study marks TIs as serious candidates for TE applications owing to band inversion-driven warping.

1 Introduction

The impressive thermoelectric (TE) performance of Bi_2Te_3 is indisputable.[1] Equipped with a valley degeneracy of $N_V = 6$ or more,[2] Bi_2Te_3-based materials have recorded some of the highest zTs near room temperature to date and have long been the material of choice for applications such as Peltier cooling of optoelectronics. The high valley degeneracy in particular has been attributed to topological properties of the material; namely, the bulk band structure becomes warped due to the strong band inversion, causing the band edges to be offset to low-symmetry k-points in the Brillouin zone.[1,3,4] Here, "warped" bands are characterized as having a non-parabolic "M" shape for the valence band and "W" shape for the conduction band (Figure 1a), as opposed to the conventional "U" shape of parabolic bands. Warped bands exhibit a valley degeneracy that is n-fold larger than a conventional parabolic band, where n is typically between 2 and 6 depending on higher order interactions.[5,6]

Previous studies have shown that the band inversion strength is a key property that determines whether bulk bands in a TI are warped (a phenomenon known as *band inversion-driven warping*) and, as a result, exhibit high valley degeneracy. In particular, bulk bands in a TI are warped when the band inversion strength is sufficiently high, as described in Refs. 5 and 6. The bands in the TI material Bi_2Se_3, for example, are not warped as evidenced by the single-valleyed electronic structure ($N_V = 1$, Figure 1b). In contrast, the bands are sufficiently inverted in Bi_2Te_3, giving rise to a comparatively higher valley degeneracy of $N_V = 6$ (Figure

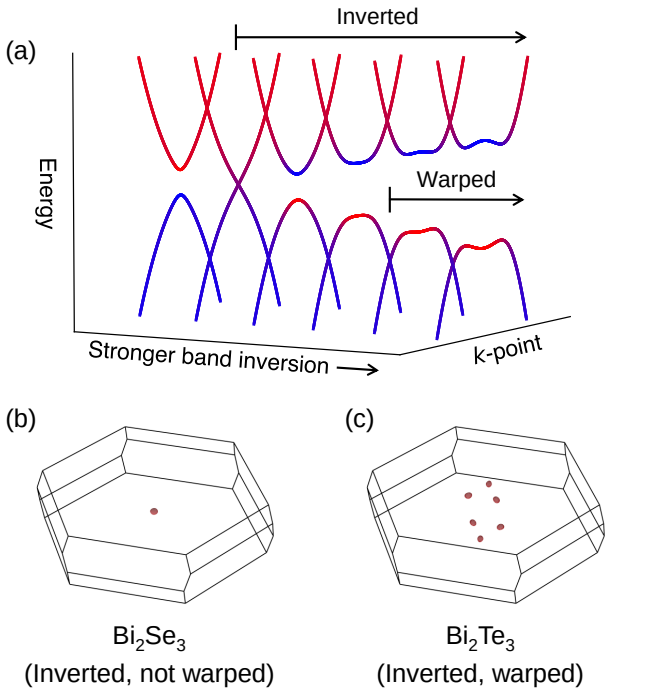

Fig. 1 Band inversion and bulk band structure. (a) Illustration of band inversion-driven warping in topological insulators. Stronger band inversion generally leads to warped bands after a critical inversion strength and, as a result, high valley degeneracy. The concept is exemplified by (b) Bi_2Se_3 and (c) Bi_2Te_3. Both compounds are topological insulators and have inverted bands; yet, the bands are not sufficiently inverted in Bi_2Se_3 resulting in a single valley ($N_V = 1$), whereas the bands are sufficiently inverted in Bi_2Te_3 resulting in warped bands and high valley degeneracy ($N_V = 6$).

[a] *Department of Materials Science and Engineering, Northwestern University, Evanston, IL 60208.*
[*] *E-mail: MichaelToriyama2024@u.northwestern.edu, jeff.snyder@northwestern.edu*

1c). The distinction can be attributed to the spin-orbit interaction which, in Bi_2Te_3, is stronger and thus leads to higher band inversion strength.[6]

The band inversion strength can be understood from the energy separation between the valence and conduction band edges at the k-point where band inversion occurs, k_0. We measure the energy separation using a quantitative parameter M_0. Mathematically (see Section 3 for more details), it is convenient to define M_0 so that $M_0 > 0$ represents noninverted bands (*i.e.*, normal insulators) and $M_0 < 0$ represents inverted bands (*i.e.*, TIs). The magnitude of M_0 is the same for both types of bands:

$$|M_0| = \frac{E_{\mathrm{CB}}(k_0) - E_{\mathrm{VB}}(k_0)}{2} \tag{1}$$

where the "VB" and "CB" subscripts refer to the valence and conduction band edges, respectively. In other words, M_0 is a measure of the direct band gap at k_0. We formally define the "band inversion strength" of a TI as the magnitude of M_0 when $M_0 < 0$. Stronger band inversion is represented by a more negative M_0 value, *i.e.*, when bands are more inverted at k_0.

TIs are particularly known for unusual properties arising from topologically-protected surface states,[7] and the influence of such surface states on TE properties have been studied quite thoroughly.[8–10] Namely, it is known that the effects of surface states are dominant at low temperatures (typically below ~150 K)[11,12] and in samples with high surface-to-volume ratio (*e.g.*, thin films[13,14] and nanograined samples[15,16]). However, the same band inversion that gives rise to surface states in TIs is also closely tied to warping and valley degeneracy (*i.e.*, features of the *bulk* band structure). As bulk effects related to topological character are relatively unknown, several key questions regarding TE properties in TIs remain to be answered. First, it has not been confirmed whether warped bulk bands of TIs are advantageous for TE performance, if at all. High valley degeneracy is beneficial for TEs when intervalley scattering is weak,[17] but given that scattering may be enhanced when multiple bands exist at the same k-point,[18] warping that results in valleys located at nearby points in k-space may also lead to high rates of scattering by, *e.g.*, phonons. Second, material properties that fundamentally link TIs to TE performance are not well-known. Though it can be hypothesized that the band inversion strength is one such property due to its relation to valley degeneracy,[6] this has not yet been confirmed through explicit analyses of TE properties. A detailed understanding may help guide material discovery efforts and band engineering strategies for high-performing TEs.

Here, we perform a detailed analysis of TE properties that result from band inversion-driven warping of bulk bands in TIs. We initially run density functional theory (DFT) calculations on the known TIs Bi_2Te_3 and Bi_2Se_3, as well as a large set of compounds crystallizing in the ZrBeSi-type structure to identify trends. We find from DFT calculations that TIs tend to exhibit higher zT than normal insulators in the same structure type; in fact, the TE performance is seemingly higher when the bands in a TI are more strongly inverted. To understand these trends, we build an appropriate model of the band structure using $k \bullet p$ theory and derive the resulting transport properties. The model indicates

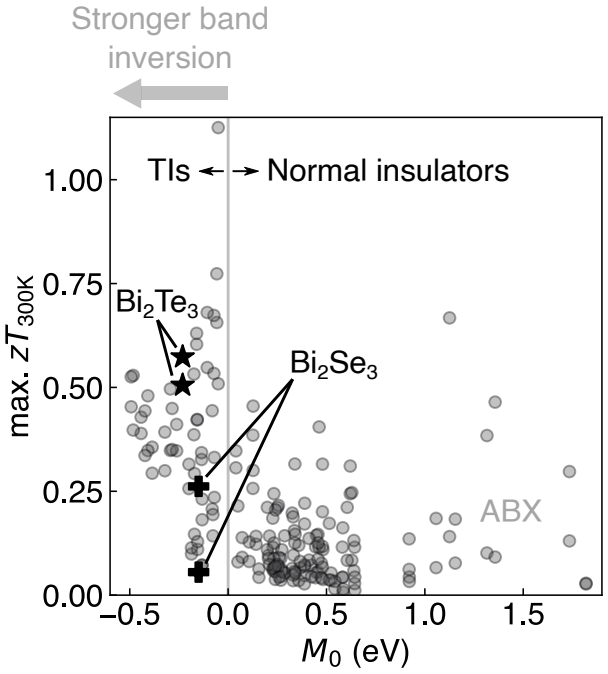

Fig. 2 Thermoelectric performance. The calculated maximum zT at 300 K (denoted "max. $zT_{300\mathrm{K}}$") for Bi_2Te_3 (star), Bi_2Se_3 (plus), and ZrBeSi-type ABX compounds (circles). The maximum zT is determined by shifting the Fermi level to the optimum doping amount. There are two points for each compound, representing n- and p-type. M_0, described by Eq. (1), is a measure of the energy separation of the band edges at the Γ-point for the present set of materials, where $M_0 > 0$ represents noninverted bands (*i.e.*, normal insulators) and $M_0 < 0$ represents inverted bands (*i.e.*, topological insulators, or TIs). More negative M_0 values represent stronger band inversion. Topological insulators seem to exhibit higher zT than normal insulators, and the TE performance appears to trend upward with more inverted bands.

that band inversion-driven warping is the phenomenon responsible for benefiting TE performance. Despite scattering events, the reduced transport mass and effectively higher valley degeneracy with warping gives rise to high zT. Moreover, the band inversion strength is found to be a key property that dictates the TE performance of TIs. We suggest design rules to engineer band inversion in TIs for improving TE performance. Our assessment confirms that TIs are indeed promising for TE applications from the perspective of charge transport in the bulk.

2 Materials survey

We evaluate the TE performances of a large set of materials by running Boltzmann transport theory-based calculations using density functional theory (DFT) and the *Ab initio* Scattering and Transport (AMSET) software.[19] The scattering rates are calculated by considering three mechanisms: acoustic deformation potential scattering, ionized impurity scattering, and polar optical phonon scattering. This is distinct from assuming a constant scattering time, which sometimes yields inaccurate predictions of transport properties.[20–22] From the scattering rates, we calculate the electrical conductivity, Seebeck coefficient, and electronic thermal conductivity. The computational details can be found in

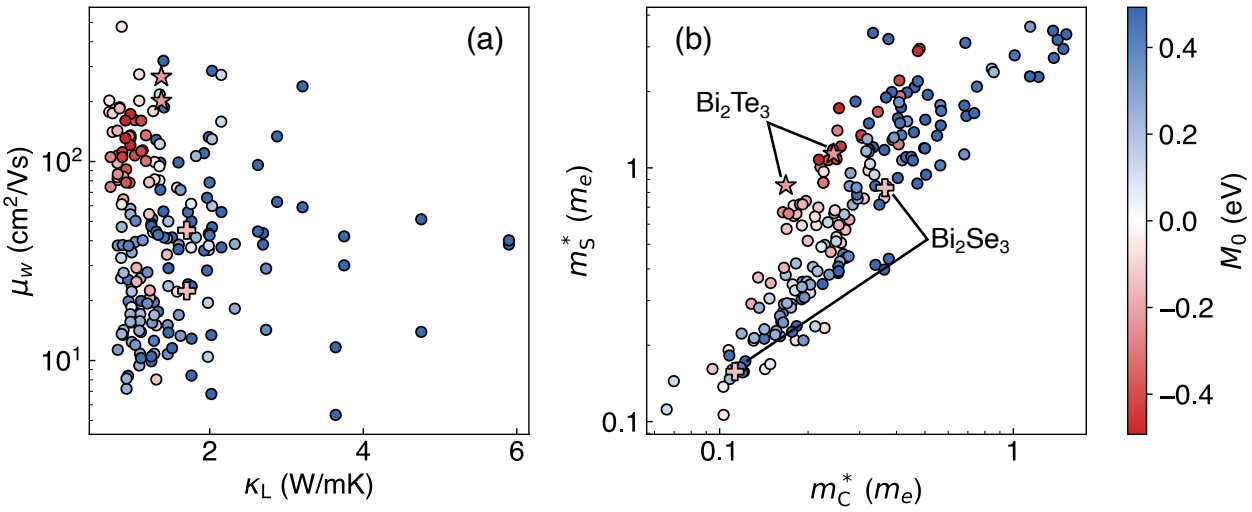

Fig. 3 Electronic and thermal properties. Material properties of Bi_2Te_3 (star), Bi_2Se_3 (plus), and ZrBeSi-type ABX compounds (circles), showing (a) weighted mobility μ_w and lattice thermal conductivity κ_L, and (b) Seebeck mass m_S^* and conductivity mass m_C^*. All properties are evaluated at 300 K and at the band edges. The color represents M_0, described by Eq. (1), where normal insulators ($M_0 > 0$) are blue and topological insulators ($M_0 < 0$) are red. Topological insulators exhibit favorable thermal *and* electrical transport properties compared to normal insulators.

the Supporting Information (SI).

The calculated transport properties of Bi_2Te_3 at 300 K are in close agreement with experimentally-measured values[1] for both n- and p-type (Figure S1). Note that we obtain good agreement when the transport properties are calculated using the experimental band gap ($E_g = 0.14$ eV) and lattice thermal conductivity ($\kappa_L = 1.37$ W/mK) at 300 K. We calculate the maximum attainable zT at 300 K (denoted "max. zT_{300K}" in Figure 2) by appropriately shifting the Fermi level to the optimum doping amount. We find, in agreement with experimental observations, that Bi_2Te_3 outperforms Bi_2Se_3 as a TE material at 300 K when optimally doped. This can partly be attributed to the warped band structure of Bi_2Te_3, which yields a comparatively higher valley degeneracy (Figure 1c) than the single-valleyed electronic structure of Bi_2Se_3 (Figure 1b). Since warping is related to the band inversion strength, the comparison between Bi_2Te_3 and Bi_2Se_3 is the first indication that materials with strongly inverted bands can attain higher zT than those with weakly inverted bands.

To perform a more meaningful comparison between TIs with varying band inversion strengths, as well as normal insulators which do not have inverted bands, a larger set of materials is needed. We therefore consider a set of $A^{+1}B^{+2}X^{-3}$ compounds (A^{+1} = Li, Na, K, Rb, Cs, Cu, Ag, Au; B^{+2} = Be, Mg, Ca, Sr, Ba, Yb, Zn, Cd, Hg; X^{-3} = N, P, As, Sb, Bi) that crystallize in the ZrBeSi-type structure (space group: $P6_3/mmc$),[23] which is known to host a variety of topological character including normal insulators and TIs.[24] Surveying the ABX compounds allows us to identify trends within the ZrBeSi structure type; due to the variety of chemistries and topological characters, we hypothesize that the conclusions drawn from the DFT calculations can extend to other structure types as well. We later develop and discuss a generalized transport model that is agnostic of the crystal structure (Sections 3 and 4), which largely validates this hypothesis. The data reported in this study are available in a public repository.[25]

We plot the maximum zT at 300 K against M_0 in Figure 2 (see the SI for computational details). From an initial survey across the diverse set of ABX compounds, we can arrive at two general observations: (i) TIs ($M_0 < 0$) tend to exhibit higher zT than normal insulators ($M_0 > 0$) within the same structure type, and (ii) the TE performance appears to be higher for TIs exhibiting stronger band inversion (*i.e.*, more negative M_0).

The variability in the data shown in Figure 2, however, calls to question which specific attributes give rise to high TE performance in TIs within a given structure type. It is often reasoned that TIs are good candidates for TEs due to the heavy elements that are typically found in TIs (*e.g.*, Bi), which tend to lower thermal conductivity.[8,26] Our results support this conclusion, as a large number of TIs (red points in Figure 3a) have an estimated $\kappa_L < 1$ W/mK, partly explaining the high zT (Figure 2). However, our calculations also strongly substantiates the value of inverted bands in TIs for electrical transport properties. The weighted mobility (μ_w) is often interpreted as a figure-of-merit for the electronic properties of TE materials.[27] The estimated μ_w (see the SI for details) are quite high for TIs, with many exceeding 100 cm^2/Vs at 300 K (Figure 3a). As a result, TIs tend to be clustered in the high μ_w – low κ_L quadrant (Figure 3a), explaining why the quality factor $B \propto \mu_w/\kappa_L$ tends to be quite high for TIs compared to normal insulators (Figure S2a). Since B provides a measure of the maximum attainable zT of a material,[28] our results show that the high zT of TIs (Figure 2) can be explained by high μ_w and low κ_L.

We inspect the electronic properties further to understand the origin of high μ_w in TIs. Namely, we compute the Seebeck effective mass (m_S^*) and the conductivity effective mass (m_C^*) from DFT calculations of the Seebeck coefficient and electrical conductivity (see the SI for details). We can express $\mu_w = \mu_0 {m_{DOS}^*}^{3/2}$, where the density of states effective mass m_{DOS}^* can be mea-

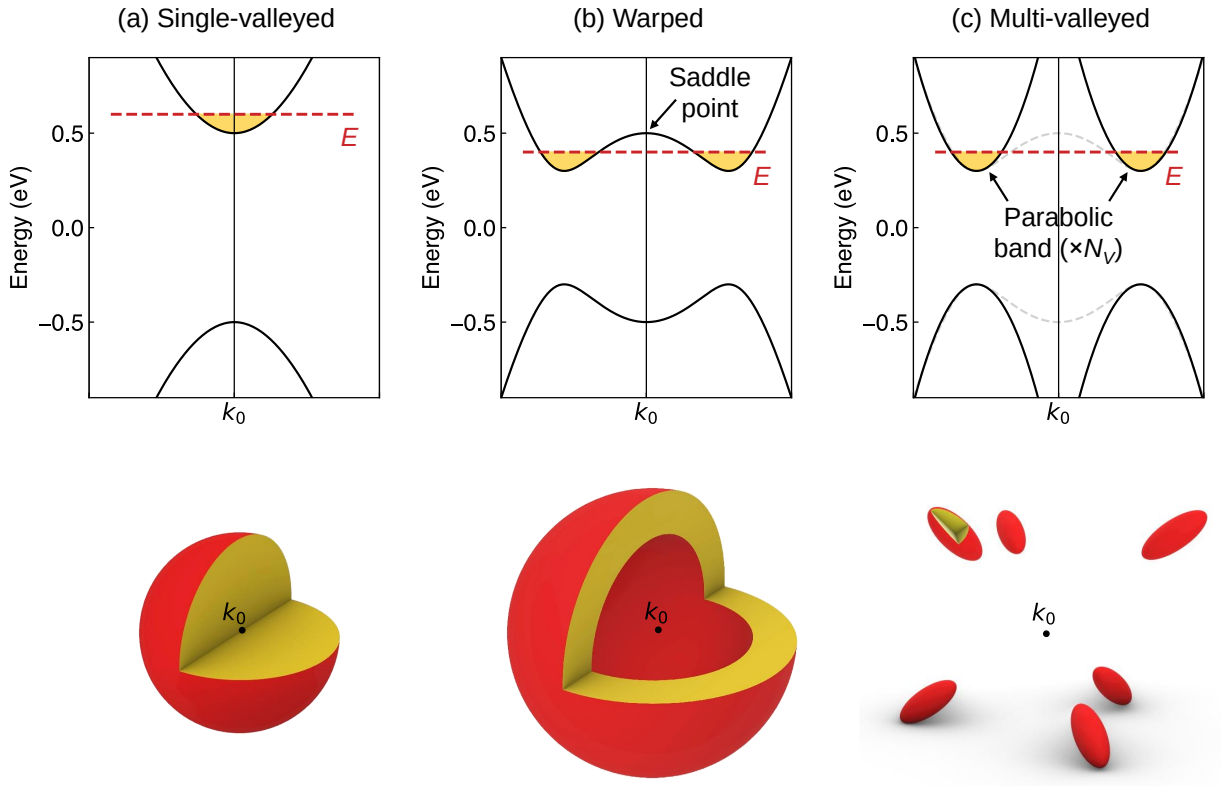

Fig. 4 Model band structures. (a) Single-valleyed band with a spherical Fermi surface, (b) warped band with a Fermi surface composed of two concentric spheres, and (c) N_V parabolic bands fitted to the band edge of the warped band. The red surface represents the Fermi surface, and the yellow regions represent occupied states. Note that in (c), N_V is dependent on the symmetry of the band inversion point, k_0, and the case where $N_V = 6$ is shown as an example.

sured by m_S^*, and the intrinsic mobility $\mu_0 \propto 1/m_C^*$. In other words, there are two main ingredients for high μ_w: high m_S^*, and low m_C^*. Many TIs in the present study exhibit such characteristics, with $m_S^* = 0.5m_e - 3m_e$ and $m_C^* = 0.1m_e - 0.5m_e$ (Figure 3b). We also evaluate the Fermi surface complexity factor $N_V^* K^* = (m_S^*/m_C^*)^{3/2}$, which can be interpreted as a metric for the effective number of carrier pockets contributing to electrical transport.[29] As expected, TIs tend to exhibit high $N_V^* K^*$ (Figure S2b), which explains the large μ_w values (Figure 3a).

The DFT calculations show that the high TE performances in TIs, within the same structure type, originate from favorable thermal *and* electrical transport properties. The high μ_w of TIs in particular can be attributed to both high m_S^* and low m_C^*, properties that are related to the bulk band structure of the material. We show in the following sections that models based on Boltzmann transport theory, which are independent of the specific structure, are consistent with the results of the DFT calculations and elucidate key features of the TI bulk band structure that generally benefit TE performance.

3 Band structure model

Charge transport properties in a material are often modeled using simplifying assumptions of the band structure and scattering mechanism of charge carriers. Commonly, the electronic structure is modeled using a parabolic band,[28,30–33] and scattering by acoustic phonons via a deformation potential is considered.[34] The drawback of the parabolic band model however is that it does not capture *warping effects* induced by band inversion in TIs. This is because the coupling between the valence and conduction band edges with secondary bands (*i.e.*, bands that are not the band edges) is not taken into account.[6]

Warped band structures can be modeled using $k \bullet p$ perturbation theory by expanding to second order in k. Here, we model the valence and conduction band edges explicitly and build an appropriate 2×2 Hamiltonian. The $k \bullet p$ Hamiltonian, assuming isotropic symmetry, takes the form

$$\hat{H}(k) = \begin{pmatrix} Ck^2 + (M_0 + M_2k^2) & Ak \\ Ak & Ck^2 - (M_0 + M_2k^2) \end{pmatrix} \quad (2)$$

where k is implicitly referenced to the k-point where band inversion occurs (for example, the Γ-point in Bi_2Te_3, Bi_2Se_3, and ZrBeSi-type ABX compounds). Note that Eq. (2) is the result of condensing the generalized $k \bullet p$ Hamiltonian, detailed in Ref. 6, to second order in k. The corresponding band structure has the form

$$E(k) = Ck^2 \pm \sqrt{(M_0 + M_2k^2)^2 + A^2k^2} \quad (3)$$

where $+$ and $-$ represent the conduction and valence band edges,

respectively. C represents the asymmetry between the band edges, where $C = 0$ indicates that the valence and conduction bands have the same form mirrored about $E = 0$. M_0 is a measure of the energy separation between the valence and conduction band edges at the k-point where band inversion occurs, as described by Eq. (1). $M_0 > 0$ represents normally-ordered bands (*i.e.*, normal insulators) and $M_0 < 0$ represents inverted bands (*i.e.*, TIs). Accordingly, Eq. (3) can model the band structure of both normal insulators and TIs. Note that we call M_0 the "band inversion strength" only when $M_0 < 0$. A is a coupling term between the valence band edge and conduction band edge. M_2 is the second-order coupling term between the band edges with secondary bands, which is necessary to capture warping effects and model the "W" and "M" shapes of the conduction and valence bands, respectively (Figure 1a).

System-specific band structure models have been developed for TIs such as Bi_2Se_3 and Bi_2Te_3,[35–37] SnTe,[5] and NaCaBi.[38] The Hamiltonian in Eq. (2) is the base form of the Hamiltonians adopted in the cases listed above, where additional parameters are necessary to satisfy symmetry constraints in specific cases. In other words, the effective Hamiltonian in Eq. (2) represents the lowest-order model needed to describe warped band structures in TIs. The main advantage of the simplified band structure model is that it permits a fully analytical derivation of the transport properties and reveals the essential physics that relates topological character to TE performance.

When the bands are inverted ($M_0 < 0$), there is a critical band inversion strength ($M_{0,c}$) that determines whether the bands are single-valleyed or warped. We define warping in terms of the curvature of the band at the k-point where band inversion occurs. For example, the conduction band is single-valleyed if the band has a "U" shape and positive curvature, and warped if it has a "W" shape and negative curvature (Figure 1a). From Eq. (3), $M_{0,c}$ is determined by the expression[6]

$$2M_2 + \frac{A^2}{M_{0,c}} = 2|C| \tag{4}$$

If $M_0 < M_{0,c}$, then the bands are warped. If $M_0 > M_{0,c}$ on the other hand, the bands are single-valleyed. In other words, even if the bands are inverted ($M_0 < 0$) in a TI, the bands must be sufficiently inverted ($M_0 < M_{0,c}$) for warping to occur.[5,6] The concept is illustrated in Figure 1a.

4 Transport model for band inversion-induced warped bands

We model charge transport properties using the standard Boltzmann transport formalism under the relaxation time approximation.[39–41] To understand the model, it is useful to recognize the Fermi surface geometry for a band described by Eq. (3), which can be either single-valleyed or warped. For a single-valleyed band, the Fermi surface is spherical for all energies, and the states inside the sphere are filled (Figure 4a). When the band is warped and the conduction band forms a "W" shape, there is a local saddle point at k_0 that is $|M_0|$ eV above mid-gap (Figure 4b). If the Fermi energy is above the saddle point, then the Fermi surface is spherical. If the Fermi energy is below the saddle point on the other hand, due to the isotropic nature of the band, the Fermi surface will consist of two concentric spheres (Figure 4b). The filled states will then occupy the volume of a hollowed sphere, as opposed to the volume of a complete sphere as in a single-valleyed band.

We refer to the transport properties derived from Eq. (3) as the "warped band transport model" (see the SI for details). The maximum zT at 300 K, which is determined by adjusting the doping level appropriately, is shown in Figure 5a as a function of M_0. Note that a particular set of values, listed in the SI, are used for the C, A, and M_2 parameters present in Eq. (3); the results qualitatively hold regardless of the specific values.

When the bands are not inverted ($M_0 > 0$, blue region in Figure 5a), the initial increase in zT with M_0 is due to the increasing band gap and, as a result, weaker bipolar conduction effects. The TE performance then stagnates at large M_0, because the TE performance at sufficiently large band gaps is limited by the properties of the majority carrier type. The overall behavior of zT when $M_0 > 0$ (*i.e.*, when the material is a normal insulator) is unsurprisingly reminiscent of a two-band transport model with parabolic valence and conduction bands.[42]

When the bands are inverted ($M_0 < 0$, yellow and red regions in Figure 5a), the TE performance increases with the band inversion strength (*i.e.*, more negative M_0). The bump in the maximum zT near $M_0 = -0.25$ in the warped region originates from scattering between the inner and outer Fermi spheres, which results in a transition from a single-peaked zT profile to a two-peaked profile. A ring-like quartic (*i.e.*, warped) band exhibits a similar two-peaked profile in the power factor.[43] A higher zT is attainable with inverted warped bands ($M_0 < M_{0,c}$, red region) than with noninverted bands ($M_0 > 0$, blue region). In fact, regardless of other details of the electronic structure, namely A and M_2 in Eq. (3), the maximum zT in most cases is higher for TIs with strongly inverted bands (Figure S3).

Together with DFT calculations (Section 2), our results provide compelling evidence that TIs are promising candidates for TEs. The utility of the warped band transport model is that it reveals how the maximum zT changes from modifications in the band structure only, since κ_L is kept constant. Notably, the model shows that M_0 is a key property that strongly influences the TE performance of a material. When $M_0 < M_{0,c}$, the band inversion strength M_0 can be interpreted as the degree to which inverted bands are warped in a TI. As a result, the model reveals that *band warping*, which is driven by band inversion, is responsible for the high zT in TIs.

5 What aspects of band warping are beneficial for thermoelectric performance?

The high zT of materials with inverted warped bands can be understood by initially examining the individual transport properties. For warped bands, the zT is higher than that of single-valleyed bands for a wide range of doping levels (Figure S4a). Since the lattice thermal conductivity is kept constant in the model, the high zT of a warped band can be attributed to the

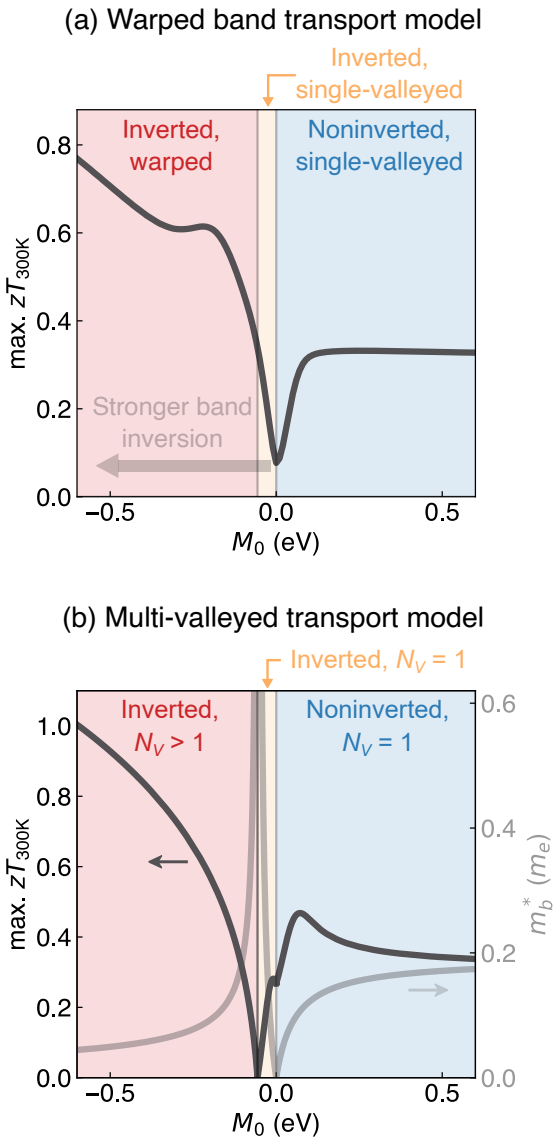

Fig. 5 Transport models. Maximum attainable zT at 300 K (denoted "max. zT_{300K}") calculated using (a) the warped band transport model and (b) the multi-valleyed transport model. M_0, described by Eq. (1), is such that $M_0 > 0$ represents noninverted bands (*i.e.*, normal insulators) and $M_0 < 0$ represents inverted bands (*i.e.*, topological insulators). Characteristics of the band structure, such as inversion and warping, are differentiated by the background shading. The results are in qualitative agreement with the trend observed in DFT calculations in Figure 2. The thermoelectric performance is higher for topological insulators exhibiting stronger band inversion (*i.e.*, more negative M_0).

high power factor (Figure S4b). The power factor is enhanced by the electrical conductivity (Figure S4c) without compromising the Seebeck coefficient (Figure S4d).

The transport properties suggest that warped bands possess characteristics of a multi-valleyed electronic structure. However, it is difficult to explicitly understand properties such as the effective mass and valley degeneracy from the warped band transport model, since the hollowed sphere-type Fermi surface of a warped band (Figure 4b) is geometrically distinct from, *e.g.*, an ellipsoidal Fermi surface. In a real material, when bands are warped due to band inversion, often the hollowed Fermi sphere breaks into a finite number of carrier pockets.[5,6] Such multi-valleyed Fermi surfaces are evident in TIs such as Bi_2Te_3 (Figure 1c) and rock-salt SnSe.[5]

In order to model a multi-valleyed band structure that still depends on band inversion in TIs, we fit a parabolic band $E = \frac{\hbar^2 k^2}{2m_b^*}$ to the edge of the band structure described by Eq. (3) as illustrated in Figure 4c. Material-specific features such as M_0 are embedded in the band effective mass $m_b^* = \hbar^2 / \left(\frac{\partial^2 E}{\partial k^2}\right)$. We subsequently derive the TE properties as if we are considering parabolic bands with valley degeneracy N_V, where $N_V > 1$ only when $M_0 < M_{0,c}$ (*i.e.*, when the bands are inverted and warped). The "multi-valleyed transport model" (see the SI for details) therefore allows us to understand the effects of band inversion on TE properties through the familiar lexicon of parabolic band transport.

For a normal insulator ($M_0 > 0$, blue region in Figure 5b), the maximum zT initially rises with M_0 because the band gap gets larger and bipolar conduction effects are suppressed. The drop in zT for larger M_0 is due to the increasing m_b^*, which lowers the electrical conductivity. Similar to Kane band transport, the monotonic relationship between the band gap and m_b^* results in a so-called "optimum band gap" for maximizing zT.[44,45] When the bands are inverted but still single-valleyed ($M_{0,c} < M_0 < 0$, yellow region in Figure 5b), the zT decreases as M_0 becomes more negative due to the increase in m_b^* and, correspondingly, decrease in conductivity. If the bands are multi-valleyed ($M_0 < M_{0,c}$, red region in Figure 5b), the TE performance enhances with stronger band inversion (*i.e.*, more negative M_0). The rising zT can be attributed to the lowering of m_b^* for the N_V parabolic bands, which improves the conductivity (Figure S5).

The maximum zT from a multi-valleyed band structure (Figure 5b) follows a profile that is similar to that of warped bands (Figure 5a), notably when the bands are sufficiently inverted ($M_0 << M_{0,c}$). Both models show that the maximum zT of a TI rises as the band inversion strength increases (*i.e.*, more negative M_0). The fitted parabolic bands within the multi-valleyed model (Figure 4c) are distinct from warped bands (Figure 4b); however, the qualitative agreement between the two models suggests that the benefits of warped bands on TE performance (as shown in Figure 5a) can be attributed to a quantity similar to m_b^*. In particular, band sharpening-like effects may be responsible for the increase in conductivity and zT with band inversion strength for warped bands (Figures 5a and S4).

We test this hypothesis by evaluating the conductivity mass (m_C^*) from properties derived from the warped band transport model (see the SI for details). m_C^*, in this way, can be interpreted as a proxy for m_b^*. Note that m_C^* is ill-defined when bipolar conduction effects are significant, and we therefore calculate the quantity for $|M_0| > 0.15$ eV. Indeed, we find that m_C^* of warped bands decreases as M_0 becomes more negative (Figure 6a), indicating that band warping indeed leads to effectively sharper bands.

We also evaluate an effective mass from the Seebeck coefficient (m_S^*) as an analogue to the density of states effective

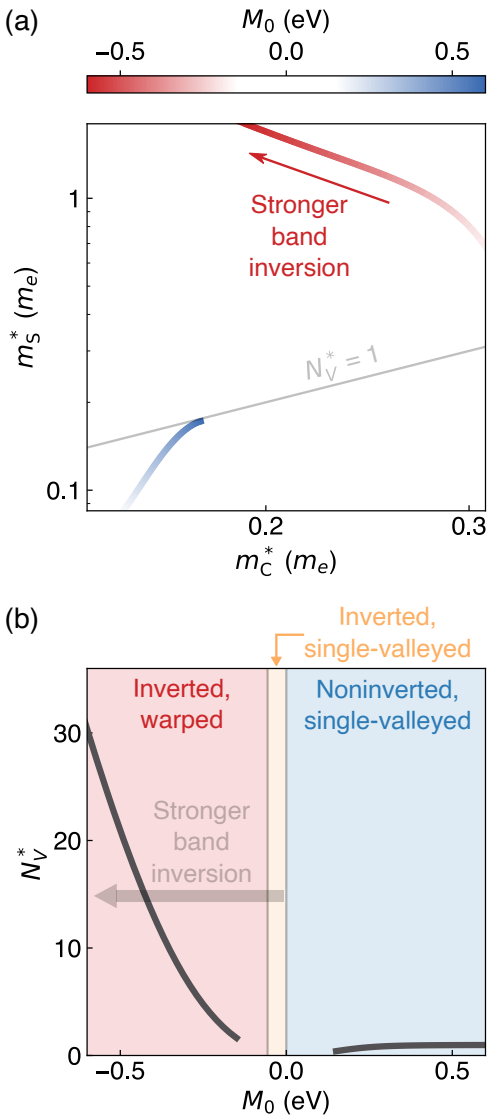

Fig. 6 Properties of the warped band transport model. (a) The Seebeck effective mass m_S^* and conductivity mass m_C^*, calculated from transport properties within the warped band transport model. The color represents M_0, where normal insulators ($M_0 > 0$) are blue and topological insulators ($M_0 < 0$) are red. (b) Effective valley degeneracy $N_V^* = (m_S^*/m_C^*)^{3/2}$ plotted against M_0. The background shading indicates characteristics of the band structure, such as inversion and warping. The high maximum zT of topological insulators can be explained by the effectively higher valley degeneracy of a warped band structure.

mass,[46] allowing us to designate an "effective valley degeneracy" $N_V^* = (m_S^*/m_C^*)^{3/2}$ to a warped band (see the SI for details). Strictly speaking, $(m_S^*/m_C^*)^{3/2}$ defines the Fermi surface complexity factor $N_V^* K^*$;[29] however, the anisotropy factor $K^* = 1$ due to the isotropic nature of the model. For a normal insulator with noninverted bands, only a single band contributes to transport. Accordingly, we find $m_S^* \approx m_C^*$ and $N_V^* \approx 1$ (Figure 6). On the other hand, warped bands possess higher m_S^* than noninverted bands, consistent with the idea of band inversion-driven high valley degeneracy.[6] Perhaps more interestingly, m_S^* monotonically increases with the band inversion strength (Figure 6a). Combined with the decreasing m_C^*, we find that N_V^* trends upward with stronger band inversion (Figure 6b).

Transport modeling therefore indicates that band inversion-driven warping leads to a combination of lower conductivity mass and higher effective valley degeneracy, which explains the rise in maximum zT with the band inversion strength for warped bands ($M_0 < M_{0,c}$). The results are consistent with DFT calculations (Section 2); materials with strongly inverted bands tend to be characterized by high m_S^* and low m_C^* (Figure 3b), explaining the high μ_w and, in part, high maximum zT. In summary, our model shows that

1. Band inversion-driven warping, which can be characterized by low conductivity mass and high effective valley degeneracy, is the critical phenomenon that leads to high TE performance in TIs, and

2. The band inversion strength is a key property that strongly influences the maximum attainable zT of TIs.

Our results so far have shown how and why the zT varies with the topological character of a material. The results can also allow us to envision design strategies to improve the TE performance by leveraging the electronic structure topology.

6 Design strategies

The results of the DFT calculations and transport modeling elucidate the critical nature of the band inversion strength in TIs. This can be attributed to the lower conductivity mass and effectively higher valley degeneracy when the bands are warped due to band inversion. In other words, by strengthening band inversion in a TI and, as a result, warping the bands, the TE performance can be enhanced. In this section, we explore ways to tune the band inversion strength in a TI.

The band inversion strength is related to the relative energy difference between the valence and conduction band edges at the k-point where band inversion occurs, as described by Eq. (1). Bands are derived from interactions between orbitals of neighboring atoms;[47] for example, the band edges at the L-point in rock-salt systems are typically derived from sp-interactions between the cation and anion.[5,48,49] Additional interactions, such as spin-orbit coupling (SOC), can also contribute significantly to band inversion in systems such as Bi_2Te_3 and Bi_2Se_3.[1,2] By tuning the interaction strength, one should expect the band inversion strength to correspondingly vary.

As a proof of concept, we show using DFT transport calculations that increasing the band inversion strength in a TI material indeed leads to an increase in the TE performance. We demonstrate this effect by tuning the SOC strength in Bi_2Se_3, following the methodology described in Ref. 6. Tuning the SOC strength relative to the normal amount at 100% correspondingly changes the band inversion strength; in particular, if the SOC interaction is stronger, then the bands at the Γ-point are more inverted. By weakening the SOC interaction, we observe a transition between having inverted ($M_0 < 0$) and noninverted ($M_0 > 0$) bands (Fig-

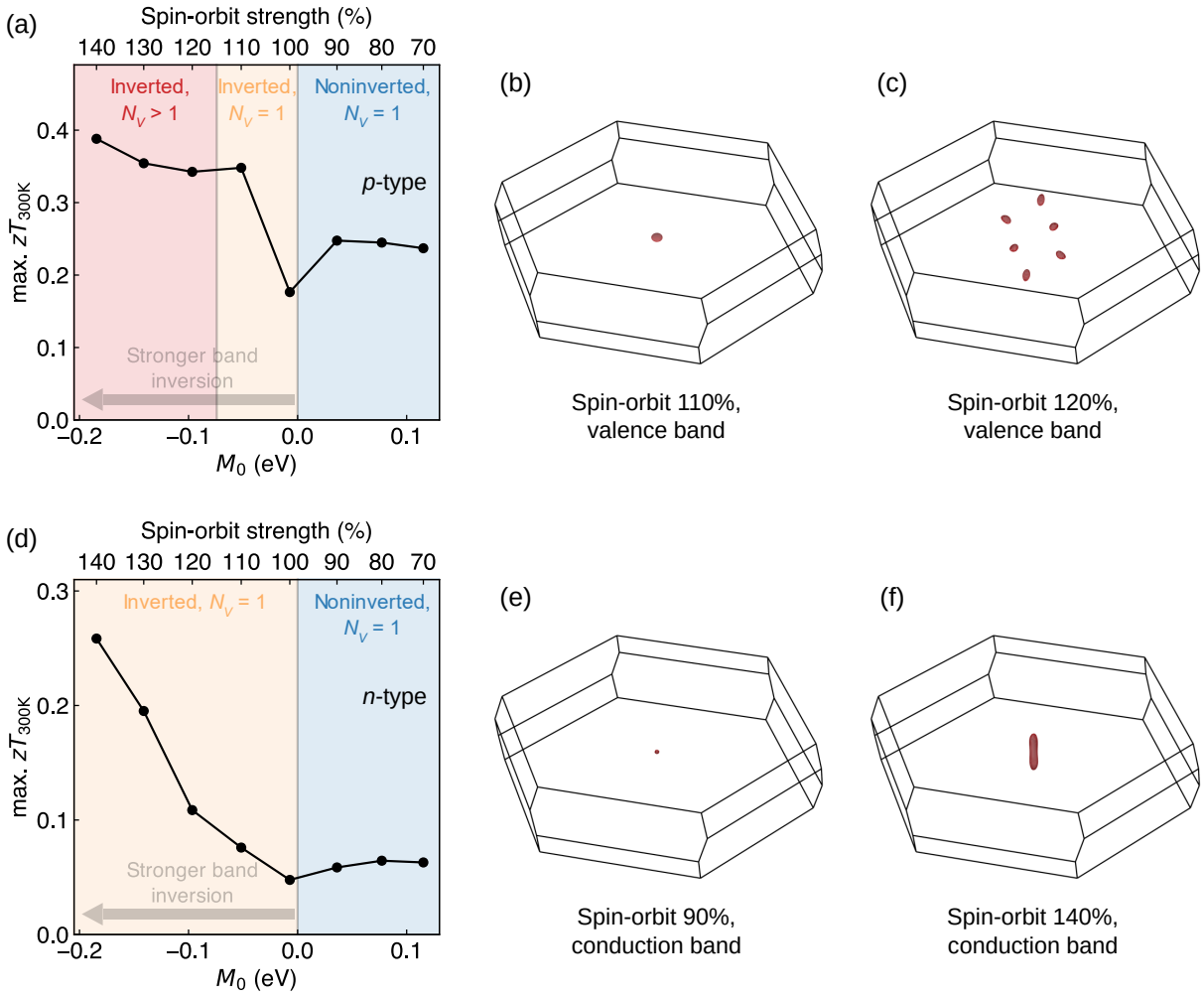

Fig. 7 Effects of spin-orbit coupling strength. The calculated maximum zT at 300 K for (a) p-type and (d) n-type Bi_2Se_3 with different spin-orbit coupling (SOC) strengths. M_0, described by Eq. (1), modulates with the SOC strength, which is listed relative to the normal amount at 100%. Fermi surfaces for the valence band are shown at (b) 110% SOC and (c) 120% SOC, *i.e.*, the boundary between single-valleyed and multi-valleyed bands despite being inverted in both cases. Fermi surfaces are also shown for the conduction band at (e) 90% SOC and (f) 140% SOC. All Fermi surfaces are calculated at 10 meV away from the band edge. These calculations show that strengthening band inversion can lead to an increase in the thermoelectric performance, thereby serving as a proof of concept for the results of transport modeling.

ure S6), allowing us to examine the TE performance across a wide range of M_0.

When the bands are inverted, increasing the SOC strength and, correspondingly, the band inversion strength leads to an enhancement in the maximum attainable zT for both p-type Bi_2Se_3 (Figure 7a) and n-type Bi_2Se_3 (Figure 7d). The zT improvement is not monotonic in p-type Bi_2Se_3 (Figure 7a), where a slight dip in zT between 110% and 120% SOC coincides with the transition between a single-valleyed and warped/multi-valleyed valence band structure (Figures 7b and 7c). Within the regime where the bands are inverted but single-valleyed (*i.e.*, the yellow regions in Figures 7a and 7d), the maximum attainable zT rises monotonically. This behavior is accompanied by an elongation of the conduction band Fermi surface with increasing SOC strength (Figures 7e and 7f). A different behavior is observed when the bands are not inverted (*i.e.*, the blue regions in Figures 7a and 7d). Namely, the maximum attainable zT initially rises with M_0 due to avoiding bipolar conduction effects, before stagnating for larger M_0. The trend in zT with the band inversion strength closely matches the results of the warped band transport model (Figure 5a).

A more direct method of modifying the band inversion strength is to strain the material. Orbital interactions are enhanced when atoms are closer together, leading to a lowering (raising) of bonding (antibonding) molecular orbitals upon compression and, as a result, stronger band inversion. We demonstrate this effect in Bi_2Te_3 by calculating the TE performance in a hydrostatically stressed state using DFT. We test strain values between -5% (compressed) and 2% (tensile-strained) to understand the trend when the atoms are both closer together and further apart relative to their equilibrium positions. There is a clear trend between the strain and optimized TE performance (Figure 8). In the compressed state, the bands at the Γ-point in Bi_2Te_3 are more inverted

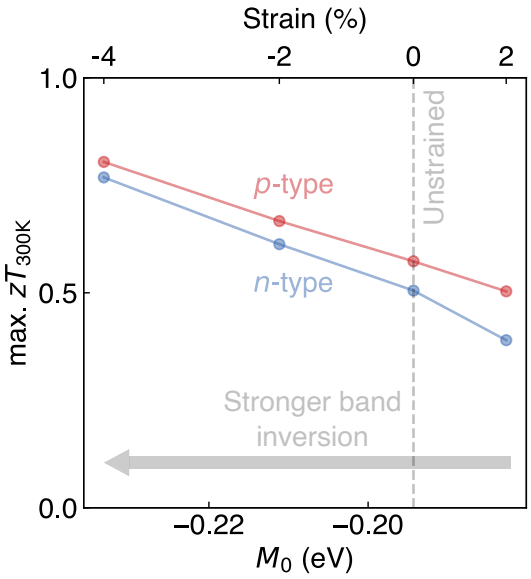

Fig. 8 Effects of strain. The calculated maximum zT at 300 K for strained n-type (blue) and p-type (red) Bi_2Te_3. M_0, which for the topological insulator Bi_2Te_3 is the band inversion strength, modulates with the hydrostatic strain in the material. The TE performance in Bi_2Te_3 can be improved by strengthening band inversion through strain engineering.

and M_0 is more negative than in the equilibrium state (Figure S7). The maximum zT at 300 K is correspondingly higher as M_0 is more negative, consistent with the results of transport modeling (Figure 5).

Of course, tuning the SOC strength and applying hydrostatic strain are idealized scenarios which neglect other effects such as the formation of native defects and plastic deformation. The analysis nonetheless serves as a direct proof of concept for attaining higher TE performance by engineering the band inversion strength. Lattice strain is often a byproduct of doping and alloying, sometimes referred to as "chemical pressure".[50] Since Bi_2Te_3 is commonly alloyed with Bi_2Se_3 or Sb_2Te_3, both of which have smaller lattice constants, it is not unreasonable to speculate that the band inversion strength is modified in part due to the compressive strain when alloyed. SOC interactions may also be affected by doping and alloying. In Bi_2Te_2Se, doping with S resulted in an increase in both electrical conductivity and Seebeck coefficient, which has been attributed to tuning the SOC.[51] It has been shown that alloying SnTe with PbTe and GeTe leads to an increase in the Seebeck coefficient for similar carrier concentrations,[52] which can be attributed to a composite effect from variations in both lattice strain and SOC strength on band inversion.

7 Conclusion

The band inversion strength is a key feature of topological insulators (TIs) that affects the thermoelectric (TE) performance. From DFT transport calculations and transport modeling, we show that TIs have the potential to perform well as TEs, and even outperform normal insulators within the same structure type. The favorable transport properties of TIs can be attributed to band inversion-driven warping, which leads to lower conductivity mass and effectively higher valley degeneracy. We predict that stronger band inversion is correlated with higher TE performance in TIs. We demonstrate this effect directly by tuning the SOC strength in Bi_2Se_3 and applying hydrostatic strain to Bi_2Te_3, both of which confirm the increase in zT with stronger band inversion. Our study not only reveals that band inversion-driven warping is the key phenomenon responsible for high TE performance in TIs, but also serves as motivation to pursue TIs as potential candidates for next-generation TE materials.

Author Contributions

M.Y.T. and G.J.S. conceived and designed this research project. M.Y.T. performed the analysis. G.J.S. supervised the project. All authors participated in preparing and editing the manuscript.

Conflicts of Interests

There are no conflicts of interest to declare.

Acknowledgements

We thank Prashun Gorai and Øven Andreas Grimnes for helpful discussions. We also thank Berhanu Snyder for helping to generate the 3D renderings of the Fermi surfaces. M.Y.T. is funded by the United States Department of Energy through the Computational Science Graduate Fellowship (DOE CSGF) under grant number DE-SC0020347. M.Y.T. also acknowledges support from the Johannes and Julia Randall Weertman Graduate Fellowship. This research was supported in part through the computational resources and staff contributions provided for the Quest high performance computing facility at Northwestern University which is jointly supported by the Office of the Provost, the Office for Research, and Northwestern University Information Technology.

References

1 I. T. Witting, T. C. Chasapis, F. Ricci, M. Peters, N. A. Heinz, G. Hautier and G. J. Snyder, *Adv. Electron. Mater.*, 2019, **5**, 1800904.
2 I. T. Witting, F. Ricci, T. C. Chasapis, G. Hautier and G. J. Snyder, *Research*, 2020, **2020**, 1.
3 H. Shi, D. Parker, M.-H. Du and D. J. Singh, *Phys. Rev. Appl.*, 2015, **3**, 014004.
4 J. P. Heremans, R. J. Cava and N. Samarth, *Nat. Rev. Mater.*, 2017, **2**, 1.
5 M. Toriyama, M. K. Brod, L. C. Gomes, F. A. Bipasha, B. Assaf, E. Ertekin and G. J. Snyder, *J. Mater. Chem. A*, 2022, **10**, 1588.
6 M. Y. Toriyama and G. J. Snyder, *Cell Rep. Phys. Sci.*, 2023, **4**, 101392.
7 M. Z. Hasan and C. L. Kane, *Rev. Mod. Phys.*, 2010, **82**, 3045.
8 N. Xu, Y. Xu and J. Zhu, *npj Quant. Mater.*, 2017, **2**, 51.
9 J. Gooth, G. Schierning, C. Felser and K. Nielsch, *MRS Bull.*, 2018, **43**, 187.
10 C. Fu, Y. Sun and C. Felser, *APL Mater.*, 2020, **8**, 040913.
11 R. Takahashi and S. Murakami, *Phys. Rev. B*, 2010, **81**, 161302.
12 P. Ghaemi, R. S. Mong and J. E. Moore, *Phys. Rev. Lett.*, 2010, **105**, 166603.

13 F. Rittweger, N. Hinsche, P. Zahn and I. Mertig, *Phys. Rev. B*, 2014, **89**, 035439.

14 N. F. Hinsche, S. Zastrow, J. Gooth, L. Pudewill, R. Zierold, F. Rittweger, T. Rauch, J. Henk, K. Nielsch and I. Mertig, *ACS Nano*, 2015, **9**, 4406.

15 G. Sun, L. Li, X. Qin, D. Li, T. Zou, H. Xin, B. Ren, J. Zhang, Y. Li and X. Li, *Appl. Phys. Lett.*, 2015, **106**, 053102.

16 S. Izadi, A. Bhattacharya, S. Salloum, J. W. Han, L. Schnatmann, U. Wolff, N. Perez, G. Bendt, I. Ennen, A. Hütten, K. Nielsch, S. Schulz, M. Mittendorff and G. Shierning, *Small*, 2023, **19**, 2204850.

17 P. Norouzzadeh and D. Vashaee, *Sci. Rep.*, 2016, **6**, 1.

18 J. Park, M. Dylla, Y. Xia, M. Wood, G. J. Snyder and A. Jain, *Nat. Commun.*, 2021, **12**, 1.

19 A. M. Ganose, J. Park, A. Faghaninia, R. Woods-Robinson, K. A. Persson and A. Jain, *Nat. Commun.*, 2021, **12**, 1.

20 E. S. Toberer, A. F. May, C. J. Scanlon and G. J. Snyder, *J. Appl. Phys.*, 2009, **105**, 063701.

21 W. Chen, J.-H. Pöhls, G. Hautier, D. Broberg, S. Bajaj, U. Aydemir, Z. M. Gibbs, H. Zhu, M. Asta, G. J. Snyder, B. Meredig, M. A. White, K. Persson and A. Jain, *J. Mater. Chem. C*, 2016, **4**, 4414.

22 Y. Katsura, M. Kumagai, T. Kodani, M. Kaneshige, Y. Ando, S. Gunji, Y. Imai, H. Ouchi, K. Tobita, K. Kimura and K. Tsuda, *Sci. Technol. Adv. Mater.*, 2019, **20**, 511.

23 X. Zhang, L. Yu, A. Zakutayev and A. Zunger, *Adv. Funct. Mater.*, 2012, **22**, 1425.

24 X. Zhang, Q. Liu, Q. Xu, X. Dai and A. Zunger, *J. Am. Chem. Soc.*, 2018, **140**, 13687.

25 https://github.com/mathtoriyama/Papers/tree/main/2023/TI_TE.

26 L. Müchler, F. Casper, B. Yan, S. Chadov and C. Felser, *Phys. Status Solidi*, 2013, **7**, 91.

27 G. J. Snyder, A. H. Snyder, M. Wood, R. Gurunathan, B. H. Snyder and C. Niu, *Adv. Mater.*, 2020, **32**, 2001537.

28 A. Zevalkink, D. M. Smiadak, J. L. Blackburn, A. J. Ferguson, M. L. Chabinyc, O. Delaire, J. Wang, K. Kovnir, J. Martin, L. T. Schelhas, T. D. Sparks, S. D. Kang, M. T. Dylla, G. J. Snyder, B. R. Ortiz and E. S. Toberer, *Appl. Phys Rev.*, 2018, **5**, 021303.

29 Z. M. Gibbs, F. Ricci, G. Li, H. Zhu, K. Persson, G. Ceder, G. Hautier, A. Jain and G. J. Snyder, *npj Comput. Mater.*, 2017, **3**, 8.

30 A. F. May and G. J. Snyder, *Materials, preparation, and characterization in thermoelectrics*, CRC press, 2017, p. 207.

31 H. Naithani and T. Dasgupta, *ACS Appl. Energ. Mater.*, 2019, **3**, 2200.

32 J. de Boor, *J. Materiomics*, 2021, **7**, 603.

33 H. Wang, R. Gurunathan, C. Fu, R. Cui, T. Zhu and G. J. Snyder, *Mater. Adv.*, 2022, **3**, 734.

34 J. Bardeen and W. Shockley, *Phys. Rev.*, 1950, **80**, 72.

35 H. Zhang, C.-X. Liu, X.-L. Qi, X. Dai, Z. Fang and S.-C. Zhang, *Nat. Phys.*, 2009, **5**, 438.

36 L. Fu, *Phys. Rev. Lett.*, 2009, **103**, 266801.

37 C.-X. Liu, X.-L. Qi, H. Zhang, X. Dai, Z. Fang and S.-C. Zhang, *Phys. Rev. B*, 2010, **82**, 045122.

38 D. Shao, Z. Guo, X. Wu, S. Nie, J. Sun, H. Weng and Z. Wang, *Phys. Rev. Res.*, 2021, **3**, 013278.

39 N. W. Ashcroft and N. D. Mermin, *Solid State Physics*, Cengage Learning, 1976, vol. 3.

40 B. M. Askerov, *Electron transport phenomena in semiconductors*, World scientific, 1994.

41 M. Lundstrom, *Fundamentals of carrier transport*, 2002.

42 M. Y. Toriyama, A. N. Carranco, G. J. Snyder and P. Gorai, *Mater. Horiz.*, 2023, **10**, 4256.

43 C. Rudderham and J. Maassen, *J. Appl. Phys.*, 2020, **127**, 065105.

44 J. O. Sofo and G. Mahan, *Phys. Rev. B*, 1994, **49**, 4565.

45 E. H. Hasdeo, L. Krisna, M. Y. Hanna, B. E. Gunara, N. T. Hung and A. R. Nugraha, *J. Appl. Phys.*, 2019, **126**, 035109.

46 G. J. Snyder, A. Pereyra and R. Gurunathan, *Adv. Funct. Mater.*, 2022, **32**, 2112772.

47 Z. Zhu, Y. Cheng and U. Schwingenschlögl, *Phys. Rev. B*, 2012, **85**, 235401.

48 M. K. Brod, M. Y. Toriyama and G. J. Snyder, *Chem. Mater.*, 2020, **32**, 9771.

49 M. K. Brod and G. J. Snyder, *J. Mater. Chem. A*, 2021, **9**, 12119.

50 K. Lin, Q. Li, R. Yu, J. Chen, J. P. Attfield and X. Xing, *Chem. Soc. Rev.*, 2022, **51**, 5351.

51 Devender, P. Gehring, A. Gaul, A. Hoyer, K. Vaklinova, R. J. Mehta, M. Burghard, T. Borca-Tasciuc, D. J. Singh, K. Kern and G. Ramanath, *Adv. Mater.*, 2016, **28**, 6436.

52 G. Xie, Z. Li, T. Luo, H. Bai, J. Sun, Y. Xiao, L.-D. Zhao, J. Wu, G. Tan and X. Tang, *Nano Energy*, 2020, **69**, 104395.